Mon. Not. R. Astron. Soc. **316**, 699–715 (2000)

Surface differential rotation and prominences of the Lupus post T Tauri star RX J1508.6–4423

J.-F. Donati,[1★] M. Mengel,[2★] B. D. Carter,[2★] S. Marsden,[2★] A. Collier Cameron[3★] and R. Wichmann[4★]

[1]*Laboratoire d'Astrophysique, Observatoire Midi-Pyrénées, 14 Avenue E. Belin, F–31400 Toulouse, France*
[2]*Faculty of Sciences, University of Southern Queensland, Toowoomba 4350, Australia*
[3]*School of Physics and Astronomy, University of St Andrews, St Andrews KY16 9SS*
[4]*Hamburger Sternwarte, Gojenbergsweg 112, D–21029 Hamburg, Germany*

Accepted 2000 March 21. Received 2000 February 16; in original form 1999 September 20

ABSTRACT

We present in this paper a spectroscopic monitoring of the Lupus post T Tauri star RX J1508.6–4423 carried out at two closely separated epochs (1998 May 06 and 10) with the UCL Echelle Spectrograph on the 3.9-m Anglo-Australian Telescope. Applying least-squares convolution and maximum entropy image reconstruction techniques to our sets of spectra, we demonstrate that this star features on its surface a large cool polar cap with several appendages extending to lower latitudes, as well as one spot close to the equator. The images reconstructed at both epochs are in good overall agreement, except for a photospheric shear that we interpret in terms of latitudinal differential rotation. Given the spot distribution at the epoch of our observations, differential rotation could only be investigated between latitudes 15° and 60°. We find in particular that the observed differential rotation is compatible with a solar-like law (i.e., with rotation rate decreasing towards high latitudes proportionally to $\sin^2 l$, where l denotes the latitude) in this particular latitude range. Assuming that such a law can be extrapolated to all latitudes, we find that the equator of RX J1508.6–4423 does one more rotational cycle than the pole every 50 ± 10 d, implying a photospheric shear 2 to 3 times stronger than that of the Sun.

We also discover that the Hα emission profile of RX J1508.6–4423 is most of the time double-peaked and strongly modulated with the rotation period of the star. We interpret this rotationally modulated emission as being caused by a dense and complex prominence system, the circumstellar distribution of which is obtained through maximum entropy Doppler tomography. These maps show in particular that prominences form a complete and inhomogeneous ring around the star, precisely at the corotation radius. We use the total Hα and Hβ emission flux to estimate that the mass of the whole prominence system is about 10^{20} g. From our observation that the whole cloud system surrounding the star is regenerated in less than 4 d, we conclude that the braking time-scale of RX J1508.6–4423 is shorter than 1 Gyr, and that prominence expulsion is thus likely to contribute significantly to the rotational spindown of young low-mass stars.

Key words: stars: activity – stars: coronae – stars: individual: RX J1508.6–4423 – stars: late-type – stars: magnetic fields – stars: rotation.

1 INTRODUCTION

By looking at the relative motion of individual spots at various latitudes at the surface of the Sun, Galileo was the first to conclude, almost 400 years ago, that the outer solar layers are rotating differentially, with the pole rotating about 20 per cent more slowly than the equator. Since then, our knowledge of the overall rotation field within the Sun has greatly improved, thanks to helioseismology in particular. We know for instance that, at a given latitude, the rotation rate is roughly constant with radius inside the convective zone, while most of the inner radiative zone rotates as a solid body. The transition between these two regimes

★E-mail: donati@obs-mip.fr (J-FD); mengelm@usq.edu.an (MM); carterb@usq.edu.au (BDC); marsdens@mail.connect.usq.edu.au (SM); acc4@st-andrews.ac.uk (ACC); rwichmann@hs.uni-hamburg.de (RW)

occurs within a thin spherical interface layer (called the tachocline) undergoing strong angular shear and playing a major role in the dynamo processes that generate the large-scale, cyclically varying, magnetic field of the Sun. For this reason, numerous modelling efforts, from both analytical and numerical sides, have been carried out to attempt to reproduce the inner rotation field of the Sun and eventually obtain a detailed description and understanding of the physical mechanisms underlying differential rotation.

However, our present knowledge of differential rotation is still very rough. Caused by the interaction between convection and rotation, differential rotation is essentially described as the result of two competing processes: viscosity (which tends to homogenize angular rotation on *spherical* shells) and meridional circulation (homogenizing angular rotation on *cylindrical* shells). Cool stars with high rotation rates (for which meridional circulation is very strong) are thus expected to show an internal velocity field very different from that of the Sun. Moreover, one can reasonably expect the dynamo magnetic field (produced by the differential rotation itself) to have a feedback effect on this differential rotation (which would then also cyclically vary in phase with the dynamo field), at least for the fastest and most magnetic rotators. Unfortunately, no seismology data such as those we have for the Sun is yet available for any stars to test these predictions, and help understand the particular case of the Sun at the same time.

We nevertheless know that cool stars other than the Sun are rotating differentially. Indeed, these stars usually host cool spots on their surface coming in and out of view as the star rotates, and thus periodically modulating the integrated light flux in the Earth direction (provided the stellar rotation axis is inclined to the line of sight and the starspot distribution is not symmetric about the rotation axis). Long-term photometric monitoring of such stars almost always indicates that the period of this modulation is slightly varying with time on a time-scale of a few years (e.g. Hall 1991); this is usually interpreted as the result of a temporal variation of the latitudinal centroid of the stellar surface brightness distribution in the presence of surface differential rotation. In addition to this, one could also invoke a temporal variation of the overall surface rotation rate caused by angular momentum redistribution as the star progresses on its activity cycle, as suggested independently by the orbital period fluctuations detected for RS CVn systems (Applegate 1992; Lanza, Rodonò and Rosner 1998). However, although this technique is very useful in suggesting the presence of differential rotation, it remains only poorly informative on what is really going on at the surface and inside the star. It cannot be used, for instance, to study quantitatively the sign of surface differential rotation, nor its evolution as the star progresses on its activity cycle.

Thanks to the new tomographic techniques designed to image the surfaces of stars from rotationally modulated spectroscopic observations, one can now reconstruct brightness maps of stellar photospheres. When coupling such imaging tools with cross-correlation-type methods like 'least-squares deconvolution' (a new technique devised by Donati et al. 1997), one can use the information from most spectral lines in the observed wavelength domain and derive brightness maps of spotted stars with unprecedented accuracy (even for stars as faint as $m_V = 11.5$; Barnes et al. 1998), thus enabling us to study the temporal evolution of such maps on short time-scales. By comparing, for instance, two images shifted by typically one week, one can in principle quantify this evolution in terms of differential rotation, in a very similar way to that used by Galileo for the Sun in the early seventeenth century. This was unambiguously achieved for the first time by Donati & Cameron (1997) on the young, rapidly rotating, dwarf AB Dor, a star about to complete its contraction towards the main sequence. They obtained in particular the rather unexpected result (recently confirmed by Donati et al. 1999) that, though rotating about 50 times faster than the Sun, AB Dor possesses almost the same level of surface differential rotation (in the sense that the equator laps the pole by one complete rotation cycle every 110 d or so) and thus the same degree of latitudinal photospheric shear as the Sun.

Long-term monitoring of this differential rotation pattern is currently being carried out to investigate whether it varies across the activity cycle of AB Dor (Donati et al. 2000). Simultaneously, and in an attempt to investigate in more detail how general this result is among cool solar-like active stars, a systematic study of differential rotation was initiated, starting first with ultrafast rotators for which Doppler imaging studies are easiest, since most data needed to reconstruct one full photospheric image can be secured in a single observing night. The first results indicate that starspot distributions tend to lose their coherence fairly quickly, on a time-scale significantly smaller than one month (Barnes et al. 1998), implying that studies of stellar differential rotation definitely need to be carried out on rather short time-scales (of the order of one week). Another very recent result indicates that one other rapidly rotating star (named PZ Tel) in an evolutionary stage similar to that of AB Dor also possesses a roughly solar amount of shear in its photosphere (Barnes et al. 2000).

The present study focuses on an even younger and faster rotator, the post T Tauri star RX J1508.6–4423 located close to the Lupus star-forming region on which several recent studies were focused (e.g. Wichmann et al. 1997, 1998). As for AB Dor, the idea underlying these new observations was to get two different Doppler images of the photosphere of RX J1508.6–4423 shifted in time by about 4 d, and look for the amount of differential rotation between them. In the next section we present the new observational material secured at the Anglo-Australian Telescope with the UCL Echelle Spectrograph in 1998 May, and the reduction procedures used to convert raw frames to stellar spectra. In Section 3, we derive new and more accurate stellar fundamental parameters for this star. The Doppler images reconstructed from our data set are then examined in detail in Section 4, and discussed in Section 5 in the particular context of surface differential rotation. We also present in Section 6 the Hα line profile variability that this star exhibits, and its interpretation as a signature for massive coronal prominences locked in corotation in the large-scale stellar magnetic field structure. We finally summarize our results and discuss their implications for our understanding of stellar convective zones and rotational braking in Section 7.

2 OBSERVATIONS

To collect our spectra, we used the UCL Echelle Spectrograph (UCLES) on the 3.9-m Anglo-Australian Telescope atop Siding Spring mountain, New South Wales, Australia. Our project was granted two telescope nights (1998 May 06 and 10) with a gap of three nights, in the specific aim of detecting differential rotation on the target star RX J1508.6–4423. The detector we selected is the new engineering grade MITLL2 CCD with 2048×4096 15 μm square pixels. Since this chip is larger than the unvignetted

Table 1. Journal of observations. The two first columns list the date and object name, while columns 3, 4 and 7 indicate the Julian date, Universal Time and fractional rotation cycle (for RX J1508.6–4423 only, using ephemeris JD = 245 0939.8 + 0.31*E*; Wichmann et al. 1998), for the first and last exposure of each sequence. Columns 5 and 6 mention respectively the total number of exposures in the corresponding sequence, and the exposure time of each exposure in the sequence.

Date	Object	JD (2,450,000+)	UT (h:m:s)	n_{exp}	t_{exp} (s)	Cycle
1998 May 06	Moon	939.8660	08:46:59	1	60	
	HD 85512	939.8808	09:08:22	1	600	
	RX J1508.6–4423	939.8945/940.3295	09:28:02/19:54:31	60	500	0.3048/1.7081
1998 May 10	HD 85512	943.8414	08:11:33	1	600	
	Moon	943.8629	08:42:36	1	60	
	RX J1508.6–4423	943.8701/943.9745	08:52:56/11:23:15	16	500	13.1294/13.4661
		944.0511/944.1136	13:13:38/14:43:36	10	500	13.7132/13.9148
		944.1785/944.2548	16:17:01/18:06:56	12	500	14.1242/14.3703

field of UCLES camera, we used a smaller window format (2048 × 2448 pixel) to reduce read-out time (down to about 90 s in normal mode). With the 31.6 groove mm^{-1} grating, up to 51 orders (numbers #81 to #131) could be squeezed on to the detector, ensuring full spectral coverage from 430 to 705 nm in a single exposure with significant overlap (as much as a half free spectral range for the bluest orders) between successive orders. Note that the reduced detector window format ensures that vignetting within UCLES camera should only be, for each order, about 10 per cent larger on both order edges than at the order centre. With a slit width of 1 arcsec, or 0.74 mm (projecting on to 3.7 pixel at the detector level), we obtained a spectral resolution of about 42 000 (i.e., 7.1 km s^{-1}) with an average pixel size of 1.9 km s^{-1}.

With this set-up, 60 successive 500-s exposures of RX J1508.6–4423 were collected on 1998 May 06 in good weather conditions (see the log in Table 1). Additional observations of spectroscopic standard stars were also recorded at the beginning of the night. The weather was significantly worse on 1998 May 10, with thin to thick high-altitude clouds interfering with our observations, and only 38 500-s exposures of RX J1508.6–4423 (gathering in three main data blocks) could be secured throughout the night. All raw frames were converted into wavelength-calibrated spectra (and associated sets of error bars) with the ESPRIT optimal extraction routines of Donati et al. (1997). Typical peak S/N of about 50 per 1.9 km s^{-1} pixel are obtained on this $m_V = 10.6$ target (see Fig. 1).

Since the Moon was up for our run, most spectra recorded on the second night include a contamination (at a few per cent level typically) from cloud scattered moonlight, that had to be removed with the help of a specific procedure. The first step of this procedure consists in forming a normalized reference spectrum of RX J1508.6–4423 (called $\mathbf{S}_*$ hereafter) by averaging together the few uncontaminated spectra of this target collected this night (around Julian date 2450 944.1). Denoting by $\mathbf{S}_\odot$ the normalized solar spectrum (reflected off the Moon) recorded the same night, we then determine the degree α to which each individual normalized spectrum $\mathbf{S}$ of RX J1508.6–4423 is contaminated by assuming that $\mathbf{S}$ can be written as a linear combination of $\mathbf{S}_\odot$ and $\mathbf{S}_*$ with respective coefficients α and $1-\alpha$ (assumed to be wavelength-independent, as expected for scattering by water clouds). A least-squares fit to the whole spectrum (except in regions where strong telluric lines are present) yields the following expression (in matrix form):

$$\alpha = \frac{{}^t(\mathbf{S}-\mathbf{S}_*)\cdot\mathbf{T}^2\cdot(\mathbf{S}_\odot-\mathbf{S}_*)}{{}^t(\mathbf{S}_\odot-\mathbf{S}_*)\cdot\mathbf{T}^2\cdot(\mathbf{S}_\odot-\mathbf{S}_*)},$$

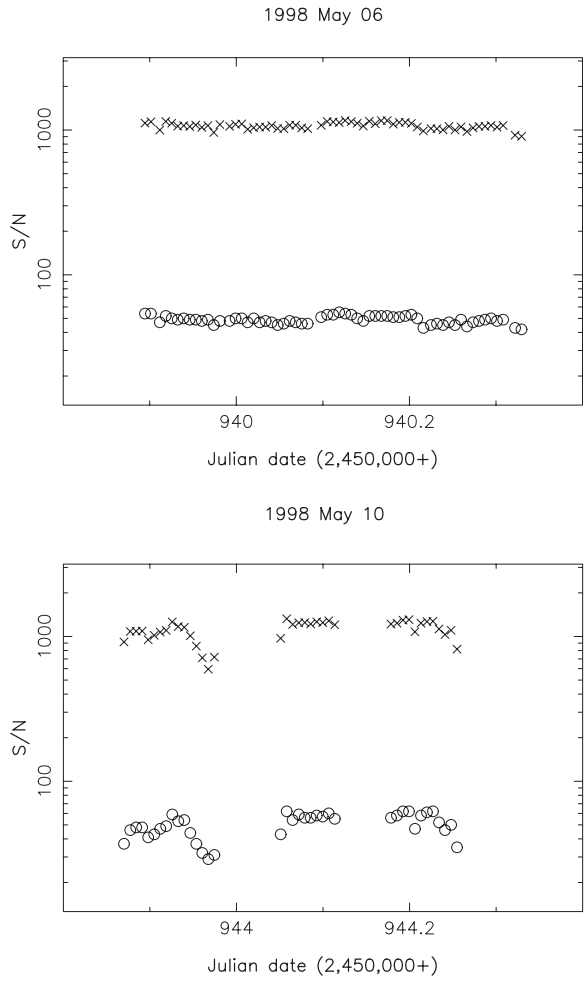

Figure 1. Peak S/N in raw spectra (○) and in LSD profiles (×) for both 1998 May 06 (top panel) and May 10 (bottom panel) data sets.

where $\mathbf{T}$ denotes the square diagonal matrix containing the inverse error bars associated with spectrum $\mathbf{S}$ (and derived by ESPRIT). Note that this procedure relies essentially on the assumption that the spectral lines of the target star are much broader than those of the contaminating spectra.

The recovered values of α are shown in Fig. 2 as a function of time. Not surprisingly, we observe that α increases when the S/N drops (and vice versa) throughout this second night. A similar

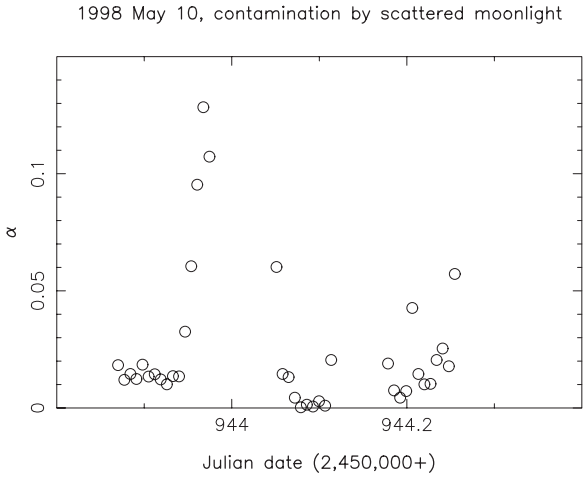

Figure 2. Degree of spectral contamination by scattered moonlight α as a function of Julian date on 1998 May 10.

procedure was used to correct the last two spectra of RX J1508.6–4423 collected at the end of the first night (during twilight), also showing significant contamination by scattered sunlight. As the degree to which our target spectra are contaminated is only moderate (always smaller than 13 per cent; see Fig. 2), the S/N degradation associated to the decontaminating process (of the order of 0.5α S/N) is therefore rather weak. This is further confirmed by the fact that the contaminated spectra can be successfully fitted down to the expected noise level, as demonstrated in Section 4.

We finally applied 'least-squares deconvolution' (LSD) (Donati et al. 1997) to all reduced spectra and obtained high S/N average line profiles of RX J1508.6–4423 at each observing epoch. With a G2 line list computed from a Kurucz (1993) $T_{\rm eff} = 5750$ K and $\log g = 4$ model atmosphere (see Section 3) and including only features with a central depth relative to continuum level larger than 0.4 (about 3000 altogether), we obtain S/N values of about 1100 per 2 km s^{-1} bin in the final LSD profiles of RX J1508.6–4423 (when normalized to a relative mean line depth of 0.7), corresponding to an average multiplex gain of 22 (see Fig. 1). The two dynamic LSD spectra we end up with are displayed in Fig. 3, and clearly exhibit signatures of cool starspots in the form of

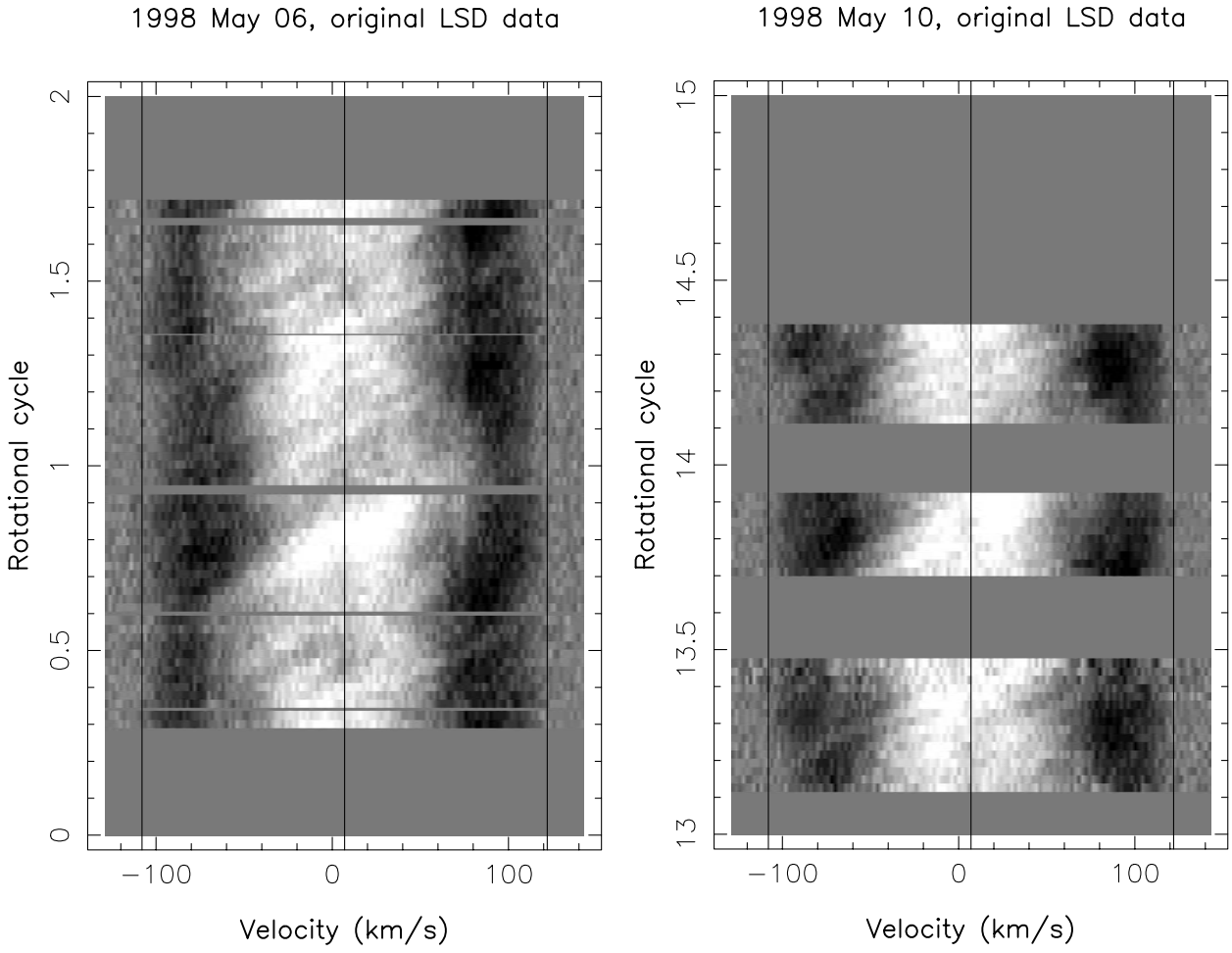

Figure 3. Trailed LSD spectrograms of RX J1508.6–4423 derived from our 1998 May 06 (left-hand panel) and May 10 (right-hand panel) observations. The three vertical lines in each plot depict the rotational broadening (on both sides) and the radial velocity (in the middle) of RX J1508.6–4423. Note that a model photospheric profile of an immaculate star with equal equivalent width, rotational broadening and radial velocity has been subtracted to emphasize the spot signatures. Rotational cycles E are computed from ephemeris JD = 245 0939.8 + 0.31E of Wichmann et al. (1998). Grey-scale levels code residuals ranging from −0.007 (black) to 0.007 (white) in units of continuum level.

profile distortions travelling from the blue to the red wing of the average spectral line. These two dynamic spectra will be discussed and analysed in detail in Section 4.

3 DERIVING FUNDAMENTAL PARAMETERS OF RX J1508.6–4423

With only moderate Hα emission (see Section 6) and no obvious near-infrared excess, RX J1508.6–4423 was first classified as a weak-line T Tauri star (wTTS), i.e., a pre-main-sequence star not surrounded by an optically thick accretion disc (Krautter et al. 1997). Since our observations show no apparent veiling nor equivalent width variations of photospheric spectral lines, we can thus confirm independently the absence of an optically thick accretion disc. From the location of RX J1508.6–4423 in the HR diagram, Wichmann et al. (1997) conclude that this star is significantly older (with an age in excess of 10^7 yr) than most classical and weak-line T Tauri stars, implying that RX J1508.6–4423 is actually what Herbig (1978) calls a post T Tauri star (pTTS) rather than a wTTS.

Being located several degrees outside the Lupus dark clouds, RX J1508.6–4423 suffers only very little interstellar extinction, implying that its $B-V$, $V-R_C$ and $V-I_C$ colour indexes (reported to be 0.69 ± 0.02, 0.41 ± 0.01 and 0.80 ± 0.01 by Wichmann et al. 1997) are well representative of its spectral type. We can confirm this point by using the photometric calibrations of Rucinski (1987), indicating that the measured $V-R_C$ and $V-I_C$ colour indexes of RX J1508.6–4423 are only 0.02 and 0.05 mag too strong, given the observed $B-V$. If we now use the synthetic $B-V$ colour indexes associated with Kurucz's (1993) model atmospheres (reported to be more accurate than previous calibration tables for solar-type stars; Morossi et al. 1993; Donati, Henry & Hall 1995), we obtain a preliminary effective temperature of about 5700 ± 50 K.

A better estimate can be derived by taking into account the small (but definite) observed reddening of RX J1508.6–4423. This reddening is mainly attributable to the cool spots producing the profile distortions we detect in the spectral lines of RX J1508.6–4423 (see Fig. 3 and Section 4). Given a photosphere-to-spot temperature contrast of about 1500 K (typical of most active stars), we infer a photospheric temperature of 5750 ± 50 K and an average spottedness of about 30 per cent of the visible hemisphere, in reasonable agreement with what we find in the next section. The synthetic $B-V$, $V-R_C$ and $V-I_C$ colour indexes associated with such a spotted star are then respectively equal to 0.70, 0.41 and 0.79, matching perfectly the observed ones. We can thus safely conclude that the effective temperature of 5309 K proposed by Wichmann et al. (1997) for RX J1508.6–4423 from the G8 spectral classification of Krautter et al. (1997) is significantly too low, and that a G2 spectral type is much more appropriate.

For a 30 per cent spottedness, the average V magnitude of 10.6 reported by Wichmann et al. (1997) for RX J1508.6–4423 translates into an unspotted V magnitude of 10.30 and thus into an absolute bolometric magnitude of 4.33 ± 0.22, given the newest distance estimate of 150 ± 15 pc for the Li-rich sample of post T Tauri stars in the Lupus star-forming region (Wichmann et al. 1999) and the bolometric correction of -0.1 corresponding to a G2 spectral type. It therefore implies that RX J1508.6–4423 has a radius of $1.22 \pm 0.12\,R_\odot$. Unsurprisingly, the Barnes–Evans relation (e.g. Beuermann, Baraffe & Hanschildt 1999) applied to a Cousins $V-I_C$ colour index of 0.72 (relevant to a $T_{\rm eff} = 5750$ K, $\log g = 4$ atmosphere; Rucinsky 1987) yields a visual surface brightness S_V of 4.90 and thus a radius of $1.30 \pm 0.15\,R_\odot$ (given the unspotted absolute V magnitude of 4.33 ± 0.22), in very good agreement with the previous result.

Comparing these values with the pre-main sequence evolutionary models of D'Antona & Mazzitelli (1994) and Forestini (1994), we derive a mass of $1.16 \pm 0.04\,M_\odot$ for RX J1508.6–4423 (implying a logarithmic surface gravity of $\log g = 4.3$) and an age of about 25 ± 10 Myr. According to these models, RX J1508.6–4423 is completing its contraction towards the main sequence, having just started to burn protons in its centre and build up a convective core. RX J1508.6–4423 thus appears as a 15 per cent higher mass analogue of the other ultrafast rotator AB Dor on which surface differential rotation was recently measured (Donati & Cameron 1997; Donati et al. 1999).

With a rotation period of about 0.31 d (Wichmann et al. 1998), RX J1508.6–4423 spins about 80 times faster than the Sun and 1.7 times faster than AB Dor, and thus appears as one of the fastest members of its class. According to Bouvier et al. (1997), the rapid rotation of stars like RX J1508.6–4423 is an indication that the star must have dissipated its accretion disc in less than 1 Myr; these models predict in particular that such stars should still be spinning up for another 10 Myr before starting to spin down to the main sequence. Note that it does not mean that such stars are not losing angular momentum, but just that the contraction time-scale (of the order of 30 Myr) is still significantly shorter than the braking time-scale.

Given the line-of-sight projected rotational velocity at the equator inferred in Section 4 (equal to $v \sin i = 115 \pm 1\,{\rm km\,s^{-1}}$), we find that the inclination angle should be $i = 35° \pm 5°$.

4 RECONSTRUCTED IMAGES

To convert the dynamic spectra presented in Fig. 3 into surface brightness images of RX J1508.6–4423, we used the stellar surface image reconstruction code of Brown et al. (1991) and Donati & Brown (1997) implementing Skilling & Bryan's (1984) algorithm for maximum entropy optimization problems. This code has been extensively applied to real data already, and the results are reported in a number of publications (Donati et al. 1992; Donati & Cameron 1997; Donati 1999; Donati et al. 1999).

The brightness imaging model we chose is that of Cameron (1992) which aims at reconstructing for each point of the stellar surface a quantity f describing the local fraction of the stellar surface occupied by spots. This quantity, varies from 0 (no spot) to 1 (maximum spottedness), and is usually referred to as 'spot occupancy'. To model the spectroscopic response of both photosphere and spots, we used LSD spectra of two very slowly rotating spectroscopic standard stars, the integrated Sun (observed through reflected moonlight) and HD 85512 as G2 and K5 templates respectively. In this context, a model profile from the whole star viewed at a given rotational phase and for a specific surface brightness image is obtained by shifting in velocity and adding up together (with adequate intensity scaling) the spectral contributions of the unspotted and spotted fractions of each elementary grid point (i.e., pixel) in the stellar image. The linear continuum centre-to-limb darkening constant used in this case is 0.60 and has been determined by a procedure similar to that described in Donati & Cameron (1997) and Barnes et al. (1998).

The surface brightness maximum entropy images of RX J1508.6–4423 derived for the 1998 May 06 and 10 data sets are

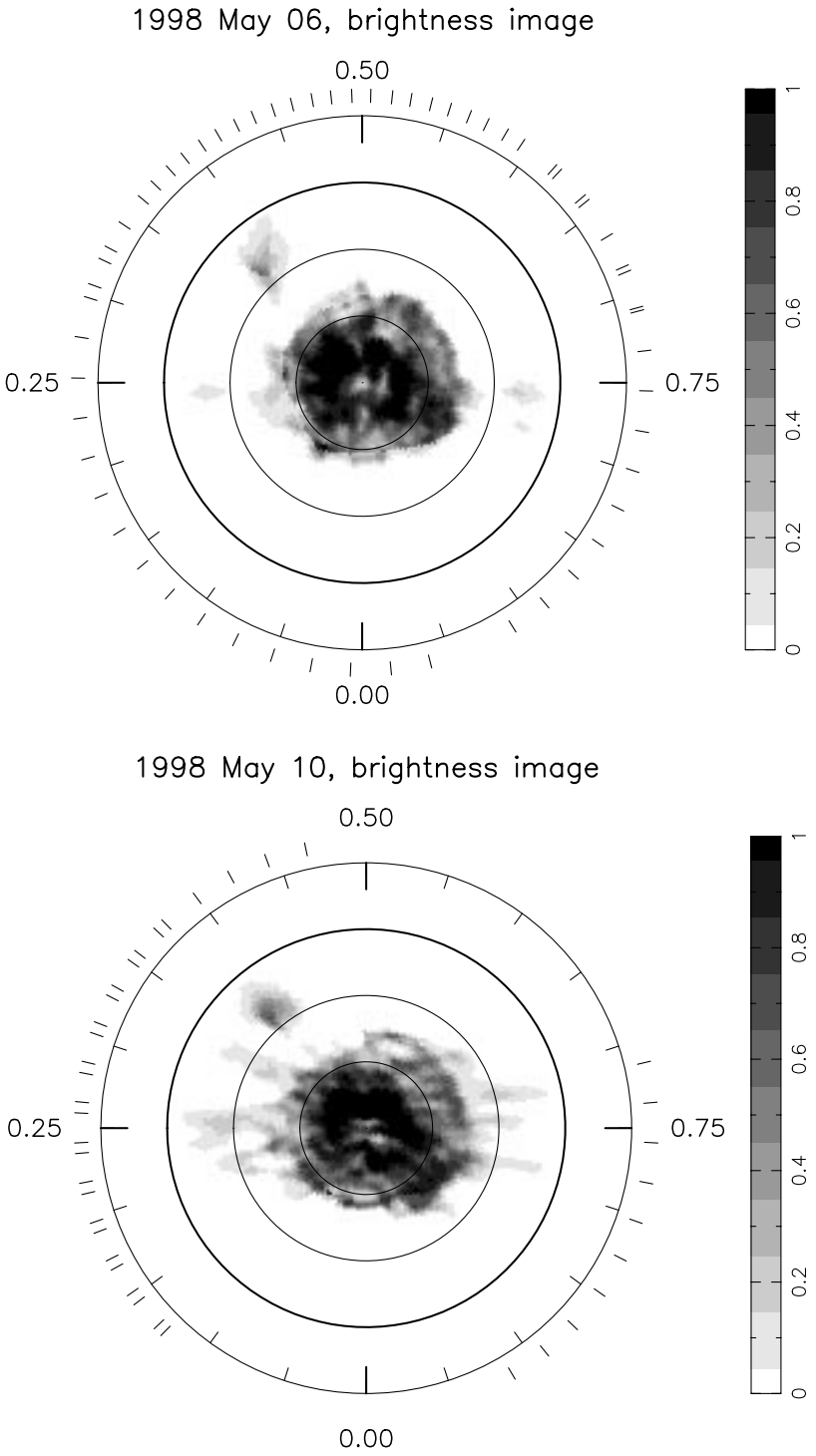

Figure 4. Maximum entropy brightness images of RX J1508.6–4423 on 1998 May 08 (upper panel) and May 10 (lower panel). These images are flattened polar projections extending down to a latitude of $-30°$ (the bold and thin circles depicting the equator and the 30° and 60° latitude parallels respectively). The radial ticks outside each plot indicate the phases at which the star was observed.

presented in the upper and lower panels of Fig. 4 respectively, while the corresponding fits to the data and associated residuals are shown (as dynamic spectra) in Figs 5 and 6. We find that the image content is minimized (i.e., the image entropy is maximized for a given reduced χ^2 threshold) for an inclination angle of the stellar rotation axis to the line of sight of $30° \pm 10°$, thus confirming independently the estimate inferred in the previous section. The same method indicates that the radial velocity of RX J1508.6–4423 is equal to $7 \pm 1\,\mathrm{km\,s^{-1}}$, in good agreement with the radial velocities of the Li-rich post T Tauri stars in the Lupus star-forming region (Wichmann et al. 1999). By minimizing systematic signatures appearing as bright/dark vertical bands just outside/inside the $[-v \sin i, v \sin i]$ velocity interval in the residual dynamic spectra in Fig. 6, we derive an optimal line-of-sight

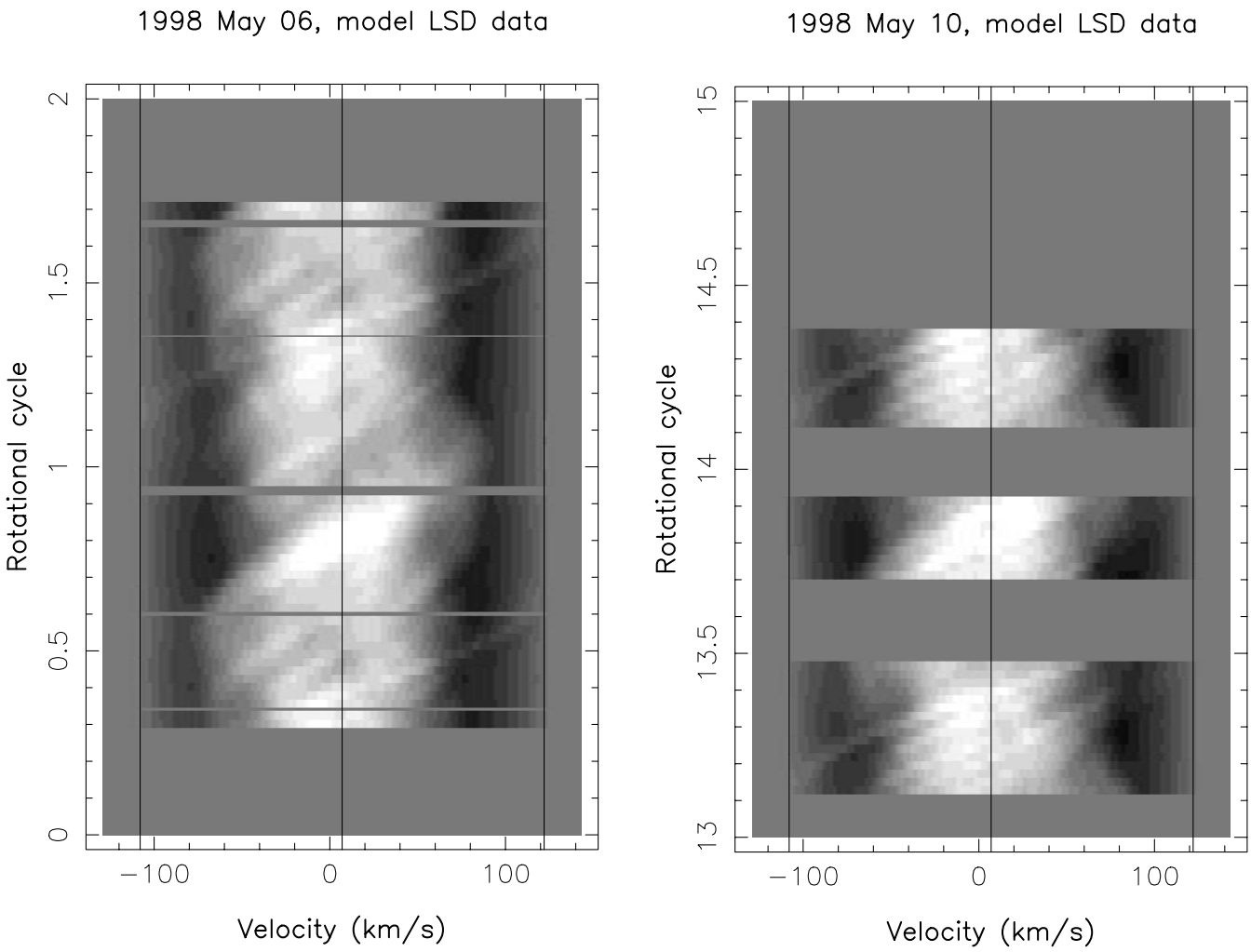

Figure 5. Maximum entropy fit to the LSD data shown in the same format as Fig. 3.

projected rotation velocity of $-115 \pm 1\,\mathrm{km\,s^{-1}}$, a couple of $\mathrm{km\,s^{-1}}$ lower than the value minimizing the information content in the brightness image. Note that the template LSD solar profile had to be scaled up by about 11 per cent to match the equivalent width of the LSD profiles of RX J1508.6–4423 (equal to $5.0\,\mathrm{km\,s^{-1}}$). Both images correspond to a unit reduced χ^2 fit to the data, and feature a total spotted area of about 18 per cent of the overall stellar surface.

As one can see from Fig. 4, the latitudinal smearing of the imaging process is, at its worst (i.e., close to the equator), of the order of 5° to 10°. It is thus comparable to that in the longitude direction (about 5°), a situation rather different from that for stars viewed at significantly higher inclination angles such as AB Dor (e.g. Donati & Cameron 1997). The reason for this is that, in low-inclination stars, low-latitude features are seen for a longer fraction of the rotation period (at the expense of seeing a smaller subequatorial portion of the stellar surface), and are thus more accurately tracked down by the maximum entropy reconstruction code.

The most striking feature of these images is the prominent cool polar spot/crown, very similar to that hosted by all other rapidly rotating stars imaged to date. The signature of this polar spot is readily visible in the dynamic spectra in Fig. 3, showing quite clearly that the observed LSD profiles are systematically shallower in the core (i.e., bright vertical bands in the centre of both panels of Fig. 3) and deeper in the wings (dark bands on the edges) than the rotational profile of an immaculate star with equal equivalent width, rotational broadening and radial velocity, i.e., that they are persistently flat-bottomed. The shape of this polar spot is very complex, with numerous appendages extending down to a latitude of 50° (e.g. at phases 0.10, 0.30, 0.55 and 0.80 in the upper panel of Fig. 4). In addition, one clear equatorial spot is reconstructed at phase 0.40 and latitude 20°. Most reconstructed features below latitude 60° repeat reasonably well between the two images. This is the case for the equatorial spot in particular showing up at almost the same phase and latitude in both maps, and to a lesser degree for the polar spot appendages at phases 0.10, 0.30, 0.55 and 0.80, which seem to have suffered some azimuthal shift to higher rotational phases.

Prior to any detailed image analysis, we have to make sure that the reconstructed surface features are real, i.e., correspond to some visible signature in the dynamic spectra in Fig. 3. As cool spots generate pseudo-emission bumps in line profiles, each reconstructed feature is expected to show up in the original dynamic spectrum as a bright trail travelling from the blue to the red wing of the profile and to larger rotational phases, as it is carried across the visible disc by rotation. The most obvious of such bright trails crosses the central vertical line in Fig. 3 at rotational cycles 0.80

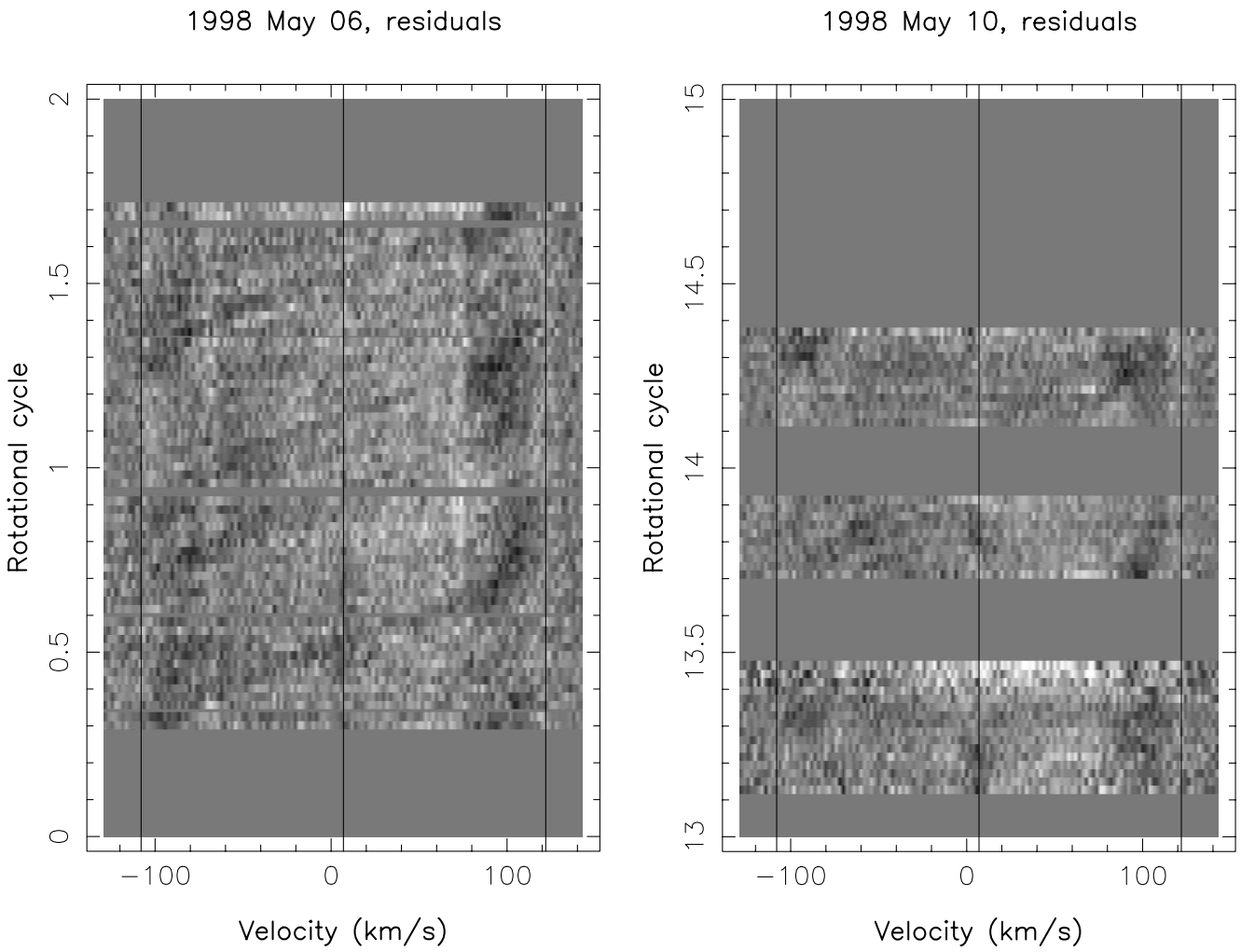

Figure 6. Residuals between observed and model LSD data shown in the same format as Fig. 3, except for grey-scale levels now coding residuals ranging from −0.004 (black) to 0.004 (white) in units of continuum level, i.e., about ±4.5 times the average error bar of LSD profiles.

and 13.85, thus validating the reality of the main polar spot appendage reconstructed between phase 0.80 and 0.90. The second major feature in the dynamic spectra is the bright blob confined to the central profile core at rotational cycles 1.30 and 13.35, and associated with the large subcomponent of the polar spot off-centred towards phase 0.30 to 0.40 at latitude 70°. Another clear bright trail, though narrower and of weaker contrast than the previous ones, can be seen crossing the line profile at rotational cycles 1.10, 13.15 and 14.15, thus confirming the existence of a polar spot appendage between phases 0.10 and 0.20 and at latitude 55°.

The track associated with the equatorial feature detected at phase 0.40 is more subtle than those from the high-latitude spots. First of all, this track is not confined to the central region of the line profile (as opposed to trails from circumpolar spots), but rather extends up to the very far line profile wings, like for instance at rotational cycles 0.5 and 1.5 in the red wing, and cycles 1.2, 13.2 and 15.2 in the blue wing. Moreover, the experienced eye will notice in Figs 3 and 5 (at rotational phases 0.40, 1.40, 13.40 and 15.40) that this track, though blended with the bright blob discussed above, is significantly *less* tilted with respect to the horizontal than those caused by polar spots, further confirming that the parent brightness feature moves faster and it thus located at lower latitudes.

We can thus safely claim that at least these five features (the polar spot, three of the high-latitude appendages and the equatorial spot) are undoubtedly real and can thus be used for a potential study on short-term variability of starspot distributions. Note that some other spots, like for instance the two reconstructed at phase 0.50 and 0.60 (latitude 50°), are probably also real (if we rely on the very faint tracks observed at rotational cycles 0.50, 0.60, 1.50 and 1.60) but are not adequately monitored on the second epoch and can thus only be marginally trusted anyway for investigations of surface differential rotation. The low-contrast features reconstructed in both maps close to the equator around phases 0.25 and 0.75 may also be real, but are definitely too weak to be used as tracers of stellar variability, given the quality of the present data set.

5 SURFACE DIFFERENTIAL ROTATION

As already briefly mentioned above, the two reconstructed maximum entropy brightness images exhibit a number of systematic differences. For instance, most of the polar spot appendages (and in particular the three identified as reliable in the previous section) tend to have moved to slightly *larger* rotational phases by the second epoch. Note that this cannot be explained simply by a slight underestimation of the rotation

period, since the equatorial feature we reconstruct also reliably looks very stable during the same time interval, implying that the stellar equator at least rotates with a period of about 0.31 d. However, one can reasonably wonder whether this apparent variability is real, and not only a result of, say, the slightly different observing conditions (and in particular the different phase sampling) between both epochs. By using the first image (better constrained than the second one thanks to a more regular and even partly redundant coverage of the rotational cycle) as the starting point when inverting the second data set, we ensure that differences between the two recovered images (and in particular spurious ones) are kept to a minimum and are dictated by the data themselves. We nevertheless present below the result of a few simple tests to convince further the reader that the variability we report is indeed real.

The very first evidence that variability indeed occurred on RX J1508.6–4423 between 1998 May 06 and 10 is that LSD profiles secured at the same rotational phase but 13 cycles apart from one another are slightly but very significantly different (with a false-alarm probability smaller that 10^{-10}), as shown in Fig. 7 in the particular case of phase 0.913. Going back to the dynamic spectra in Fig. 3, we can indeed check visually that the main bright trail centred at phase 0.80 (and therefore the corresponding surface brightness feature) shifted as a whole towards larger rotational phases.

Another possible test is to generate a model dynamic spectrum for the second observing epoch assuming that the brightness distribution did not change (i.e., by using the well-constrained image derived from the first data set), and compute the residuals with respect to the observed dynamic spectrum at the second epoch. The resulting image, shown in Fig. 8, has an overall reduced χ^2 of 1.9 (for a total number of independent data points of about 1300), demonstrating that the model dynamic spectrum does not reproduce the observed data to the noise level (with a false-alarm probability smaller than 10^{-10}). This residual image exhibits a number of clear features that were not present in the previous residual image in Fig. 6, the most obvious one being the trail crossing the profile at rotational cycle 13.85. From the structure of this trail (with the bright strip in front of the dark one), we infer that the corresponding brightness surface feature shifted towards larger rotational phases, thus further confirming the conclusion of the previous paragraph.

Altogether, it suggests that, while the equatorial feature at phase 0.40 rotated at a rate close to the nominal rotation period of 0.31 d, the main polar spot appendage at phase 0.80 and latitude 50° built up a phase delay of about 0.05 cycle in 13 cycles. To make this result more quantitative, the first way to proceed is to cross-correlate latitude belts between both images in Fig. 4, as was done for AB Dor for instance by Donati & Cameron (1997). Thanks to the low stellar inclination angle i of RX J1508.6–4423 (which allows us to see all stellar longitudes down to a latitude of 30° at each rotation phase) and to the fact that no low-latitude features are present in either of the two May 10 data set phase gaps, the whole phase range can be safely used in the cross-correlation process. The result, shown in Fig. 9, indicates that the cross-correlation peak is well defined all the way from a latitude of about 15° to a latitude of about 60°. In particular, it definitely confirms our earlier presumptions that RX J1508.6–4423 rotates faster at low latitudes. By cross-correlating latitude belts on restricted phase intervals, we can check that the correlation peak at low latitudes is (as expected) due to the equatorial spot at phase 0.40, while the broader peak at latitude 50° is mostly due to the

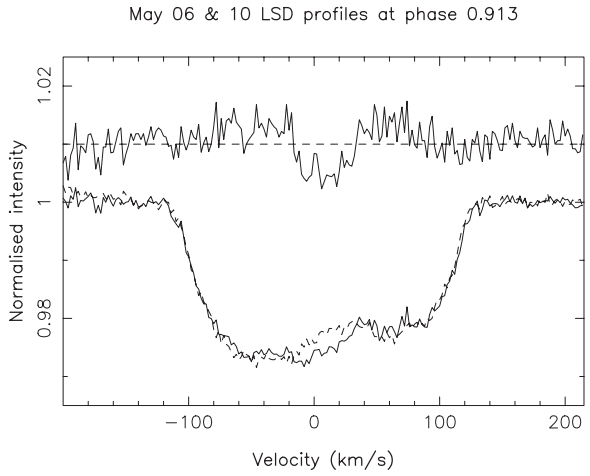

Figure 7. LSD profile of RX J1508.6–4423 at rotational cycles 0.9113 (lower curves, full line) and 13.9148 (lower curves, dashed line). The difference between the two profiles (expanded twice and shifted upwards by 1.01) is also shown (upper curve, full line).

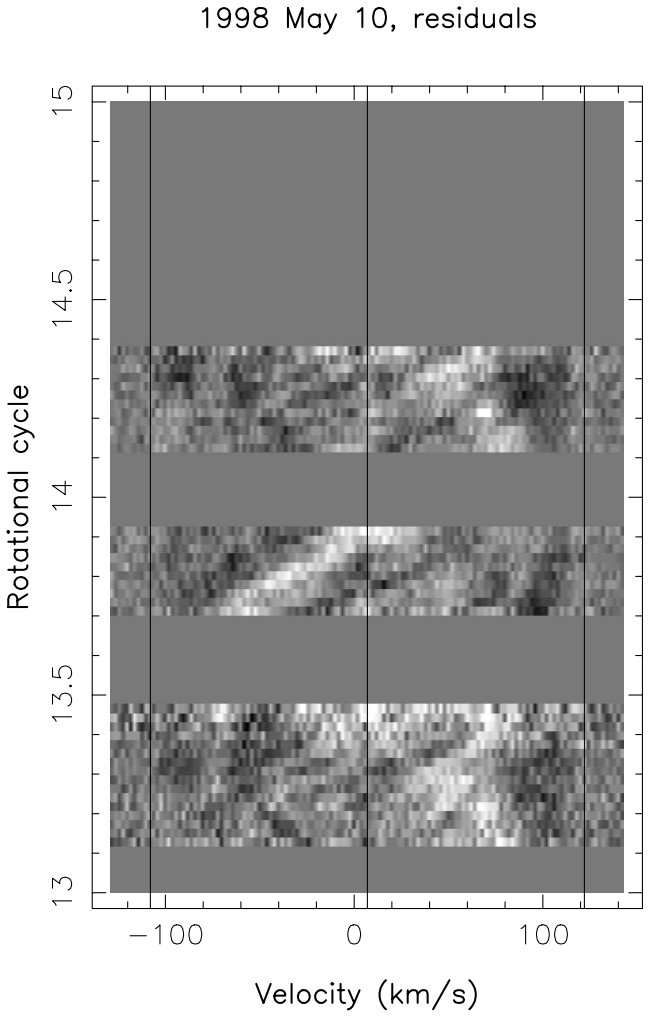

Figure 8. Same as the right-hand panel of Fig. 6, except that the model LSD profiles were computed using the brightness image reconstructed from the May 06 data set.

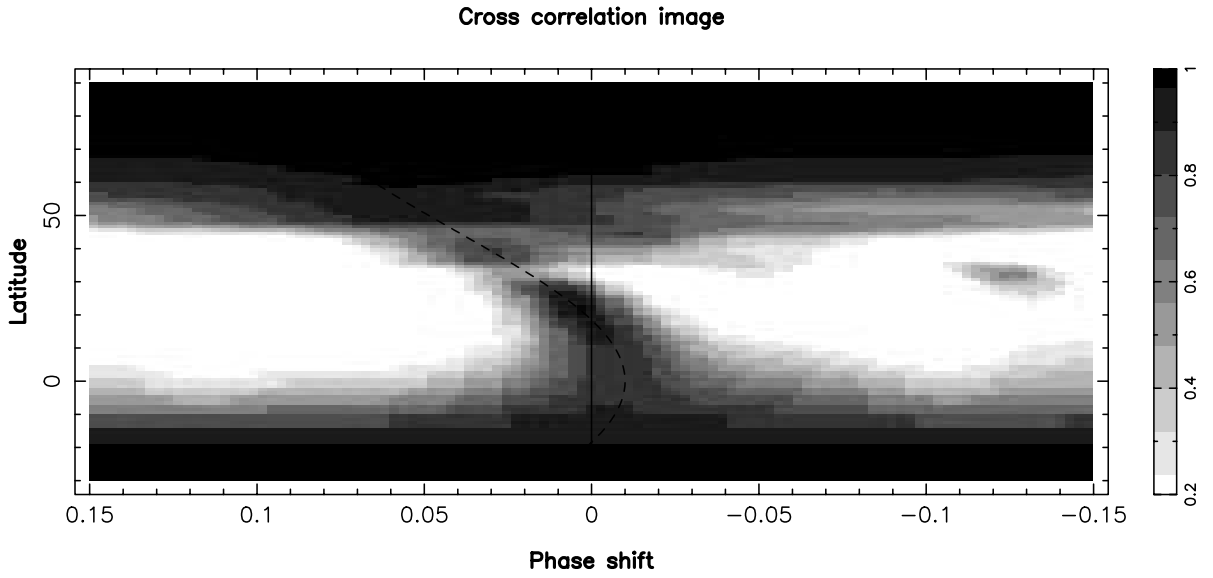

Figure 9. Cross-correlation image obtained by cross-correlating latitude belts of both images in Fig. 4. The dashed line is a visual $\sin^2 l$ fit (with l denoting the latitude) to the cross-correlation peak.

main polar spot appendage discussed extensively in the previous paragraphs.

Fig. 9 also demonstrates that the differential rotation we detect on RX J1508.6−4423 is compatible with a solar-like law (i.e., with a rotation rate decreasing towards high latitude proportionally to $\sin^2 l$, where l denotes the latitude) between latitudes 15° and 60°. Assuming that such a law can be extrapolated to all latitudes, we find (from a visual fit to the cross-correlation image) the following latitudinal dependence of Ω:

$$\Omega(l) = 20.28 - 0.15 \sin^2 l (\mathrm{rad\,d^{-1}}).$$

Note that latitude smearing in the maximum entropy reconstruction process, being only moderate in the particular case of RX J1508.6−4423 (see Section 4), is not expected to reduce significantly the differential rotation signal by more than a few per cent.

A second method of quantifying the amount of differential rotation is to take one of our two maximum entropy images (e.g., the May 06 one) and evolve it to the other observing epoch (i.e., May 10), assuming a given surface differential rotation law in the form

$$\Omega(l) = \Omega_{\rm eq} - \mathrm{d}\Omega \sin^2 l (\mathrm{rad\,d^{-1}}),$$

where $\Omega_{\rm eq}$ and $\mathrm{d}\Omega$ denote respectively the rotation rate at the equator and the rotational shear between the equator and the pole. Both $\Omega_{\rm eq}$ and $\mathrm{d}\Omega$ are considered as free parameters, varying respectively from 20.15 to 20.45 $\mathrm{rad\,d^{-1}}$, and from 0.0 to 0.30 $\mathrm{rad\,d^{-1}}$. For each pair of $\Omega_{\rm eq}$ and $\mathrm{d}\Omega$, we construct an evolved version of the original image, and evaluate how well the corresponding synthetic profiles fit the data set originally secured for this other epoch (i.e., May 10) by computing the associated reduced χ^2. The corresponding χ^2 maps as a function of the assumed differential rotation parameters $\Omega_{\rm eq}$ and $\mathrm{d}\Omega$, are shown in Fig. 10.

Not surprisingly, the minimum reduced χ^2 value achieved over the whole parameter range significantly exceeds unity. It only reflects that a maximum entropy image obtained through a unit reduced χ^2 fit to a given data set will not fit a higher S/N (or equivalently a more extensive) data set at the same χ^2 level, thanks to the very principle of maximum entropy image reconstruction. In particular, it does *not* imply that the assumed differential rotation model is unable to account entirely for the observed variability, as will be demonstrated in the following paragraph (by exhibiting one image that can fit both data sets to the noise level simultaneously in the framework of this model).

The reduced χ^2 maps in Fig. 10 first indicate that $\Omega_{\rm eq}$ and $\mathrm{d}\Omega$ are strongly correlated along a direction of equation $\Omega_{\rm eq} - 0.52\,\mathrm{d}\Omega$. It tells us in particular that the latitude at which the rotation rate is best determined is such that $\sin^2 l = 0.52$, i.e., $l = 46°$ (the rotation rate at this latitude being 20.21 ± 0.01 $\mathrm{rad\,d^{-1}}$). This is, of course, the direct consequence of the fact that the surface feature producing the largest spectral signature (i.e., the main polar spot appendage at phase 0.80; see Section 4) is located close to this latitude. The reduced χ^2 vary along this direction as well, thanks to the low-latitude feature reconstructed at phase 0.40. Although the variation in this direction is weaker than in the perpendicular one (due to the fact that this equatorial spot generates smaller profile distortions), it is nevertheless significant.

Given the number of independent data points involved in the reduced χ^2 computation (of the order of 1300 for the left-hand panel and 2300 for the right-hand panel of Fig. 10), we conclude that the 68.3 per cent confidence region in the $\Omega_{\rm eq}$ and $\mathrm{d}\Omega$ parameter space is defined as the region enclosing all parameter pairs for which the reduced χ^2 does not exceed the minimum value by more than 1.8 and 1.4 per cent respectively. The values and error bars we get for $\Omega_{\rm eq}$ and $\mathrm{d}\Omega$ for both plots in Fig. 10 are equal to 20.27 ± 0.02 and 0.11 ± 0.04 $\mathrm{rad\,d^{-1}}$, and 20.285 ± 0.015 and 0.13 ± 0.03 $\mathrm{rad\,d^{-1}}$ (for the left- and right-hand panels respectively). The average values and error bars are 20.28 ± 0.01 and 0.12 ± 0.02, in reasonable agreement with the estimates obtained from the visual fit to the cross-correlation image.

The ultimate method to determine the amount of differential rotation at the surface of RX J1508.6−4423 is to merge all our 98 LSD profiles in a *single* data set and reconstruct brightness images

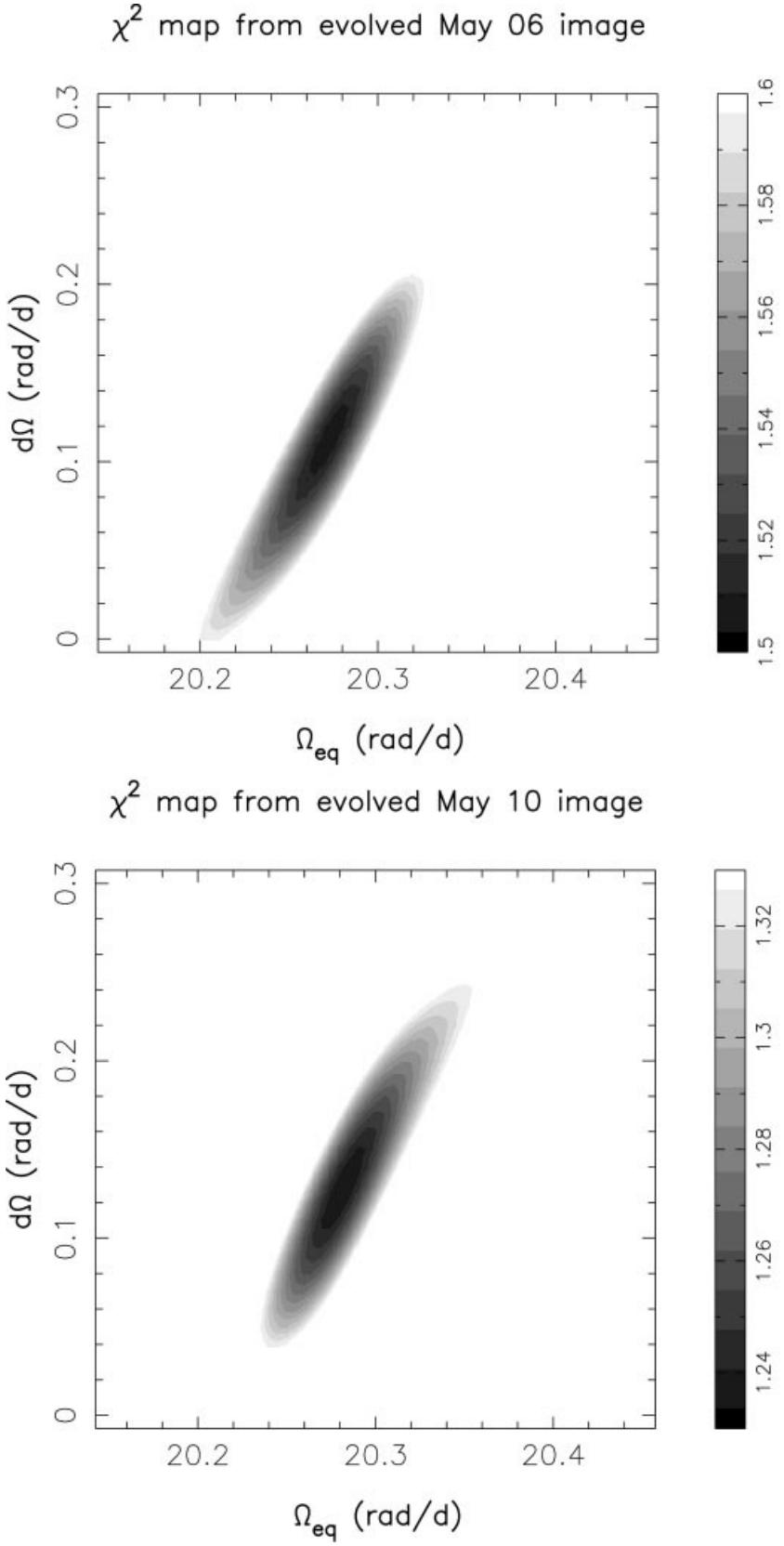

Figure 10. Reduced χ^2 maps obtained by evolving a given image with our differential rotation model and comparing the corresponding synthetic data set to that measured at the other observing epoch, as a function of equatorial and differential rotation rates Ω_{eq} and $d\Omega$. The upper panel (lower panel) corresponds to the May 06 (May 10) image evolved forward (backward), and whose synthetic data set is compared to that recorded on May 10 (May 06). Darker grey-scale levels correspond to smaller reduced χ^2.

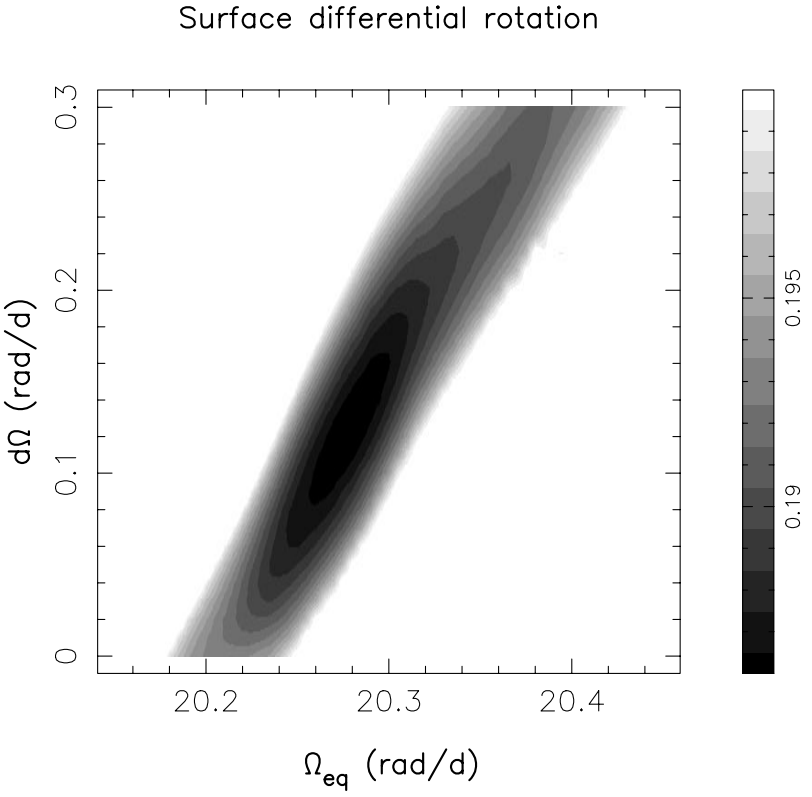

Figure 11. Image spottedness as a function of equatorial rotation and photospheric shear rates Ω_{eq} and $d\Omega$. Note that LSD profiles (from *both* observing nights) were used simultaneously to reconstruct a single brightness image per Ω_{eq} and $d\Omega$ pair. Brighter grey-scale levels represent increasing image spottedness (with black and white depicting image spottedness smaller and larger than 18.6 and 20.0 per cent respectively) and thus less probable differential rotation parameters. Images showing up as white on this plot correspond to models that did not converge properly (i.e., for which the data could not be fitted within the noise level).

assuming the same surface differential rotation law as for the previous test. For each pair of Ω_{eq} and $d\Omega$, we reconstruct one brightness map through a unit reduced χ^2 maximum entropy fit to the data (see Fig. 11). First of all, the fact that we can fit the global data set down to the noise level for at least some values of Ω_{eq} and $d\Omega$ tells us that the intrinsic variability detected on RX J1508.6–4423 can entirely be explained in the framework of our differential rotation model. Moreover, we can conclude that the likeliest differential rotation law compatible with the data is that minimizing the information content (i.e., the total spottedness) of the reconstructed image. We find that Ω_{eq} and $d\Omega$ are respectively equal to 20.28 ± 0.01 and 0.13 ± 0.02 rad d^{-1} (error bars being estimated through Monte Carlo simulations), in good agreement with the values found in the previous paragraph.

Altogether, we can thus conclude that RX J1508.6–4423 rotates differentially, and that the observed differential rotation is compatible with a solar-like law, at least in the range of latitudes (i.e., 15° to 60°) where distinct surface brightness spots can be used as tracers of the plasma flow. Assuming that this differential rotation law can be extrapolated to all latitudes, we find that the equator of RX J1508.6–4423 does one more rotational cycle than the pole every 50 ± 10 d, implying a photospheric shear 2 to 3 times stronger than that of the Sun.

6 PROMINENCES

Hα is always in emission on RX J1508.6–4423 (with an average equivalent width of about 0.2 nm) and exhibits most of the time a double-peaked profile. The dynamic spectra corresponding to our two observing epochs, shown in Fig. 12, feature two vertical bands at velocities of about ± 180 km s^{-1} with respect to the stellar radial velocity (7 km s^{-1}), as well as a number of structures crossing from the blue to the red band (e.g., at rotational cycles 0.45, 0.80 and 1.45) or in the other direction (e.g., at rotational cycle 1.00). Since the whole pattern of the dynamic spectrum repeats quite well from one rotational cycle to the next, we conclude that most of the Hα emission is due to circumstellar material locked in corotation with the stellar surface. Note that a similar, though much weaker, modulation pattern is (barely) visible in Hβ, indicating that the Balmer decrement of the emitting gas is steep, i.e., that these emission lines are optically thin.

The most obvious interpretation is that this emission is due to massive prominences trapped in the large-scale magnetic field of RX J1508.6–4423 forming out at a distance of about 1.3 to 2.0 R_* (i.e., mostly at the corotation radius located at $1.65 \pm 0.10\,R_*$), a situation similar to that of AB Dor where such coronal structures were first discovered. The main difference with the clouds surrounding AB Dor, however, is that these prominences (which tend to be centrifugally confined to the equatorial plane in such ultrafast rotators) are not seen crossing the disc on RX J1508.6–4423, given the low axial inclination (30° to 35°) of this star, and thus never show up as absorption transients as on AB Dor. Moreover, thanks to their closer distance to the star and their higher overall mass (compared to those orbiting around AB Dor),

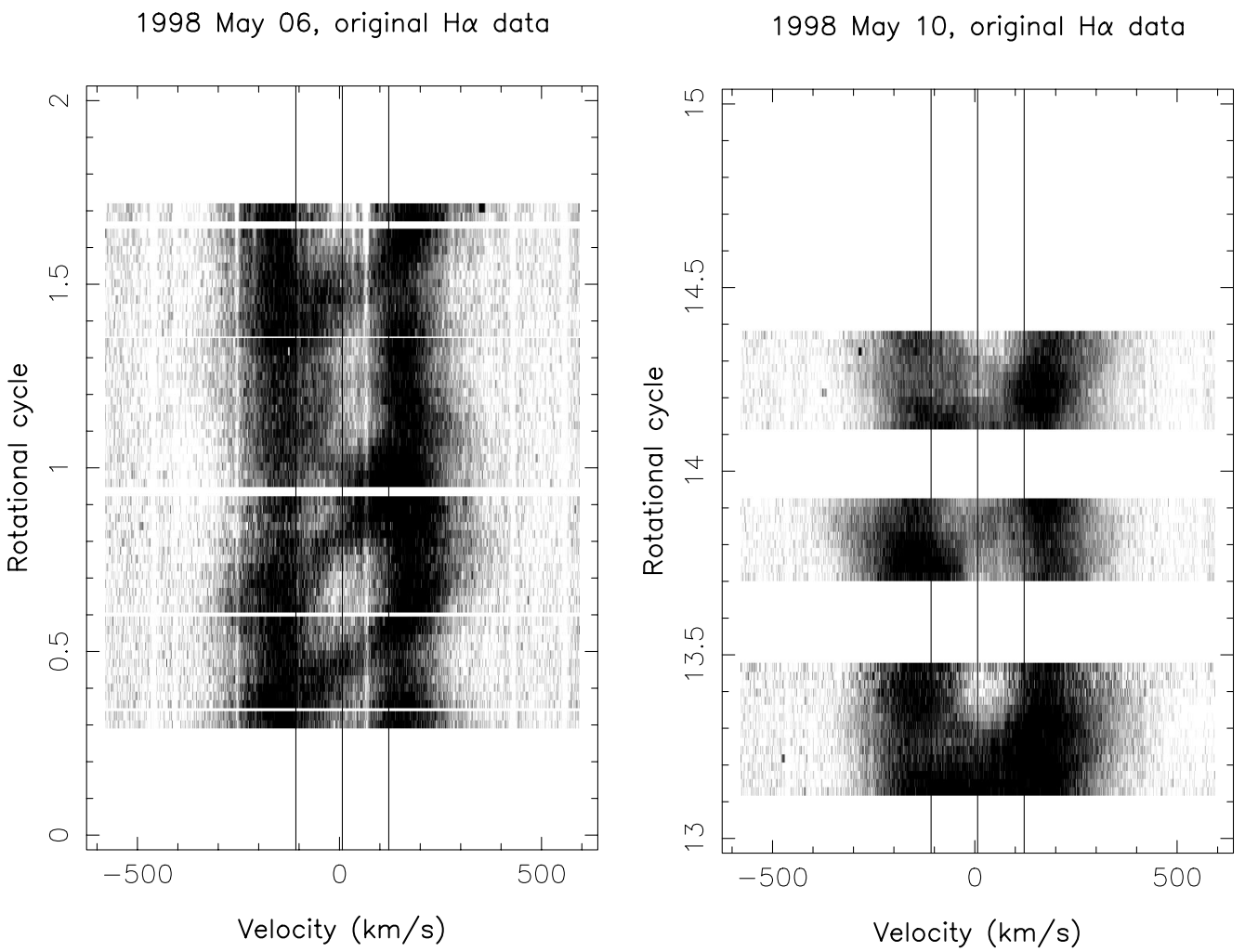

Figure 12. Trailed Hα spectrograms of RX J1508.6–4423 derived from out 1998 May 06 (left-hand panel) and May 10 (right-hand panel) observations. Vertical lines have the same meaning as in Fig. 3. Grey-scale levels code intensity levels ranging from 1.0 (white) to 1.2 (black) in units of continuum level.

these prominences are observed all the time as emission features, as discussed more extensively in Section 7.

We used the maximum entropy tomographic technique of Marsh & Horne (1988) to convert the Hα dynamic spectra in Fig. 12 into Doppler maps (in velocity space) of the Hα-emitting circumstellar environment of RX J1508.6–4423, under the assumption that this environment is rotating synchronously with the stellar surface. In this context, the distance of a cloud from the stellar rotation axis is directly proportional to its orbital velocity; Doppler maps in velocity space thus represent a straightforward image of the *spatial* distribution of the Hα-emitting material trapped in the stellar magnetic loops. Not surprisingly, the resulting tomograms (presented in Fig. 13) are found to be very weakly sensitive to the exact shape of the model local emission profile (set here to a Gaussian with a Doppler width of 0.04 nm), since the profiles of all clouds are dominated by rotational broadening. The maximum entropy fits to the observed profiles are shown as dynamic spectra in Fig. 14. The reconstructed Doppler maps show in particular that a complete ring of prominences encircles the star at the corotation radius at both epochs, producing the above-mentioned vertical bands in both sets of dynamic spectra. In addition to this ring, we also observe a few denser condensations at specific rotational phases (0.45 and 0.85 at the first epoch, and 0.05, 0.55 and 0.80 at the second epoch), tracing out complete sinusoids in the trailed spectrograms. A detailed comparison of Figs 12 and 14 demonstrates that our model captured most of the information present in the original data.

If the circumstellar ring of Hα-emitting gas is structurally similar at both epochs, the location of the denser condensations changed radically between 1998 May 06 and 10. Note that this variability is once again real and not attributable to some misbehaviour of the tomographic technique used, as it is directly visible from the spectral signatures of these denser condensations (the emission transients crossing the line profile in both directions) in Fig. 12. This probably implies that the whole prominence system observed on the first epoch was ejected and replaced by a similar one in a period of less than 4 d. We think that this short-time-scale variability mostly results from a local reorganization of field lines up in the corona, rather than to a rapid evolution of the magnetic topology at photospheric level, for at least two reasons. First, we demonstrate in Section 5 that the photosphere suffered nothing more than a slight differential rotation-induced shear within the same time interval, implying that the typical time-scale characterizing the evolution of the photospheric spot distribution is much longer than 4 d. Moreover, it looks as if the rotational

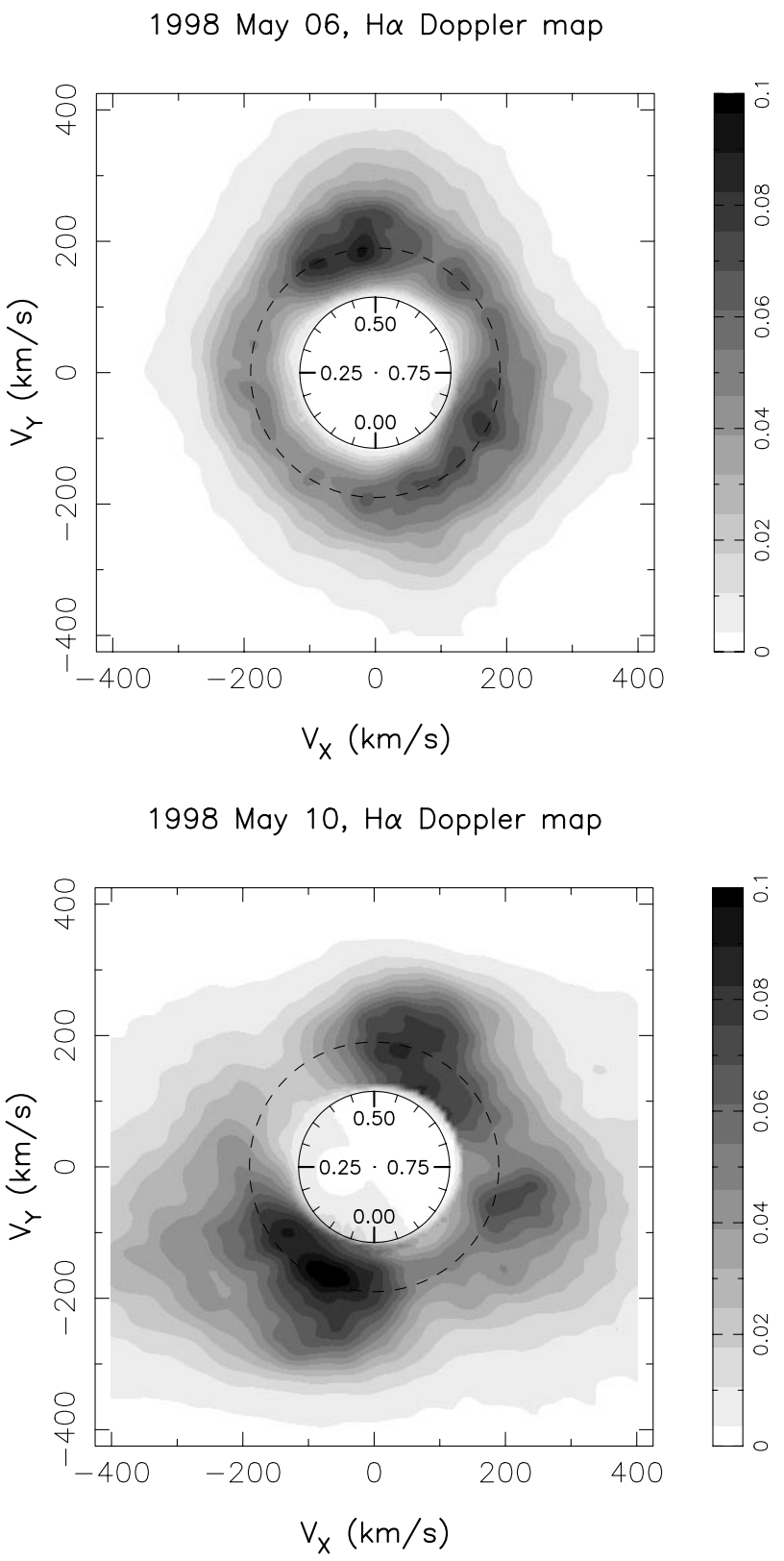

Figure 13. Maximum entropy brightness Doppler maps of the Hα-emitting circumstellar material around RX J1508.6–4423, as reconstructed from our 1998 May 06 (upper panel) and May 10 (lower panel) data sets. The inner circle (full line) depicts the central star and the outer one (dashed line) the corotation radius. Note that some of the elongated shape of the lower map may be spurious, due to gaps in the phase coverage (between phases 0.50 and 0.70, and phases 0.95 and 0.10). Darker grey-scale levels represent stronger local Hα surface brightness above the continuum, from 0 (white) to 0.1 (black) in units of pm per 8 km s^{-1} square pixel (for the local Hα equivalent width), or equivalently from 0 (white) to 2.8×10^{-17} (black) in units of erg s^{-1} cm^{-2} per μas^2 (for the local Hα surface brightness).

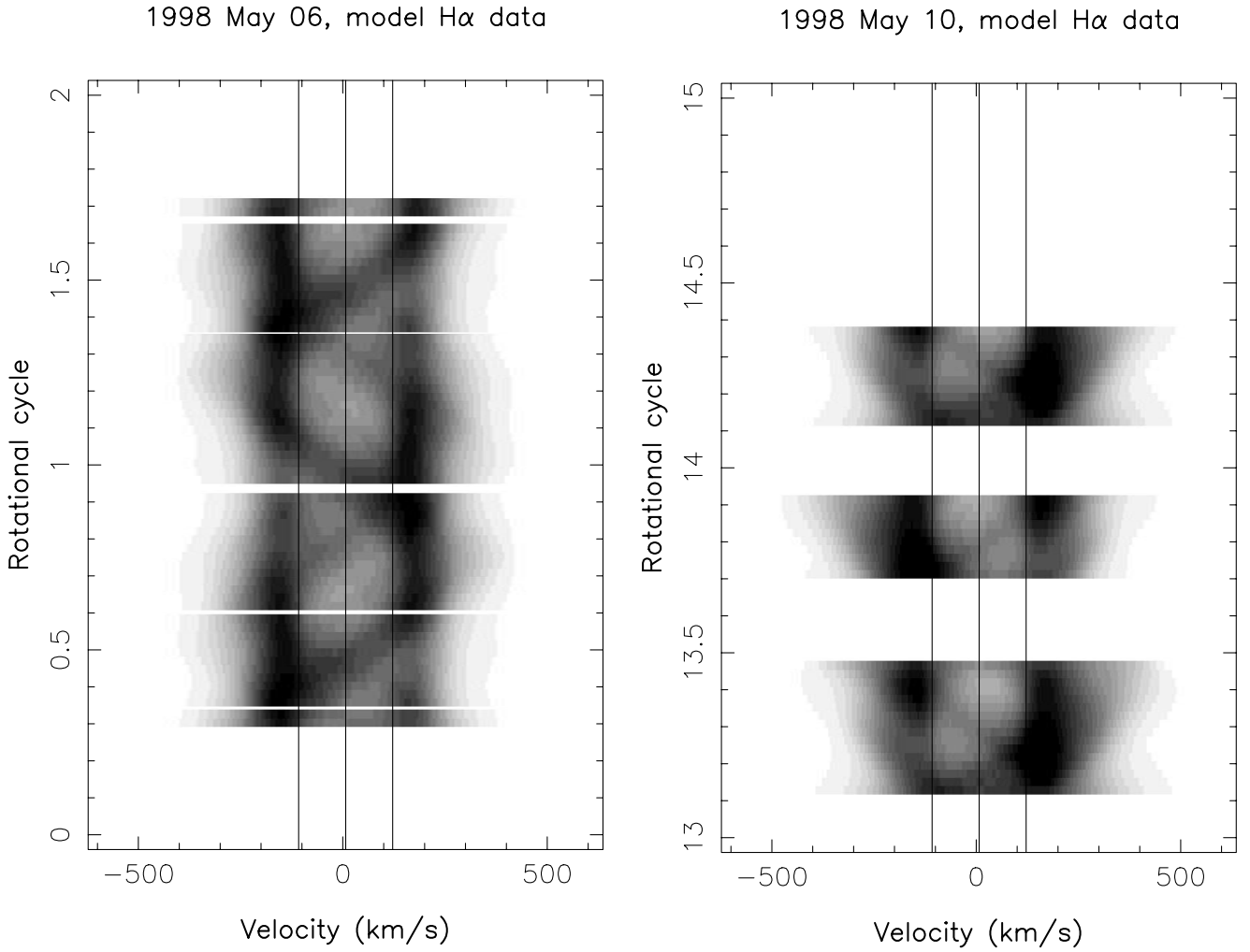

Figure 14. Maximum entropy fits to the observed Hα data, shown in the same format as Fig. 12.

phases at which the denser condensations form in the corona all correspond rather well to that of brightness features reliably identified in Section 4. Note that a similar conclusion was obtained for AB Dor by Donati et al. (1999) from a simultaneous spectroscopic/spectropolarimetric monitoring of the photospheric field topology and the prominence system.

7 DISCUSSION AND CONCLUSIONS

We presented in this paper a spectroscopic monitoring of the post T Tauri star RX J1508.6−4423 carried out at two closely separated epochs (1998 May 06 and 10) with the UCL Echelle Spectrograph on the 3.9-m Anglo-Australian Telescope. Applying stellar surface imaging techniques to the least-squares deconvolved sets of spectra, we show that this star features on its surface a large cool polar cap with several appendages extending to lower latitudes, as well as one spot close to the equator. The images reconstructed at both epochs are in good overall agreement, except for a significant photospheric shear that we interpret in terms of latitudinal differential rotation. Given the spot distribution at the epoch of our observations, differential rotation could be investigated only between latitudes 15° and 60°. We find in particular that the observed differential rotation is compatible with a solar-like law (i.e., with rotation rate decreasing towards high latitudes proportionally to $\sin^2 l$, where l denotes the latitude) in this particular latitude range. Assuming that such a law can be extrapolated to all latitudes, we find that the equator of RX J1508.6−4423 does one more rotational cycle than the pole every 50 ± 10 d, implying a photospheric shear 2 to 3 times stronger than that of the Sun. Another way of saying it is that the rotation period could potentially vary between 0.3098 and 0.3118 d from the equator to the pole. If our result is correct, rotation periods determined from photometric observations should thus always fall within this range. This is the case at least for those of Wichmann et al. (1998).

Though stronger than solar, the photospheric shear we report on RX J1508.6−4423 is definitely not strong enough to support an earlier suggestion by Smith (1994) that T Tauri stars possess extremely strong differential rotation (with an equator rotating about twice as fast as the pole), and that the reason for the bimodal distribution in the rotation periods of T Tauri stars was (in this context) that classical and weak-line members of this class tend to form spots at high and low latitudes respectively. Our results also demonstrate at the same time that spots of weak-line T Tauri stars such as RX J1508.6−4423 are clearly not restricted to low latitudes, as proposed by Smith (1994). On a similar topic, the present paper establishes unambiguously that stars rotating as fast

as 80 times the solar rate (RX J1508.6−4423 is actually the most rapidly rotating single star imaged to date) can still form spots close to the equator. This is in strong contradiction with the models of Schüssler et al. (1996) predicting that magnetic flux tubes rising from the base of the convective zone should break the surface at high stellar latitudes under the common action of buoyancy and Coriolis forces.

Being both the most rapidly rotating and most massive star on which differential rotation has been reliably estimated, RX J1508.6−4423 is also that showing the strongest photospheric shear measured to date. Given the small stellar sample for which such measurements are available, it is probably premature to derive any reliable conclusion about how differential rotation varies with stellar fundamental parameters. We can nevertheless stress that our new observations are at least in qualitative agreement with the recent theoretical prediction of Kitchatinov & Rüdiger (1995, 1999) claiming that photospheric shear should increase with mass at constant equatorial rotation rate.

We also discovered that the Hα emission profile of RX J1508.6−4423 is most of the time double-peaked and strongly modulated with the rotation period of the star. We interpret this modulated emission as being due to a dense and complex prominence system encircling the star at a distance of about 1.3 to 2.0 R_*, i.e., mostly at the corotation radius (located at $1.65 \pm 0.10\,R_*$). As opposed to those orbiting around AB Dor (which only show up as absorption transients crossing the stellar line profile from blue to red), these prominences are observed all the time as emission features, tracing complete sinusoidal paths in the trailed Hα spectrograms (see Figs 12 and 14).

The average emission fluxes measured in the three first lines of the Balmer series (estimated from the mean RX J1508.6−4423 spectrum after subtraction of the rotationally broadened, radial velocity shifted solar spectrum) are respectively equal to 10× and 2×10^{-13} erg s^{-1} cm^{-2} for Hα and Hβ. Note that this flux includes both the contribution from the chromosphere and the prominences (no flares were observed on RX J1508.6−4423 during our two observing nights). Both contributions can be estimated separately on the assumption that the corresponding regions are spatially distinct (prominences concentrate on a torus centred at $1.65\,R_*$, while the chromosphere does not extend further out than $1.1\,R_*$) and are corotating with the stellar surface (ensuring that signatures in dynamic spectra from emission regions at different distances from the rotation axis are spectrally distinct). In this context, we find that the flux contribution from prominences to Hα and Hβ are respectively equal to 5× and 0.5×10^{-13} erg s^{-1} cm^{-2}, while the chromospheric flux contribution to these two lines is about 5× and 1.5×10^{-13} erg s^{-1} cm^{-2}. The corresponding Hα/Hβ Balmer decrements for the prominences and chromosphere are thus respectively equal to 10 (typical for weak solar prominences; Stellmacher & Wiehr 1994) and 3.3 (usual for chromospherically active stars at quiescence; e.g. Montes et al. 1999). This therefore confirms that the emitting plasma has physical properties similar to that of weak solar prominences (in agreement with the conclusion reached in Section 6), and that the light we get from the prominences is essentially caused by radiative recombination of H atoms photoionized by the stellar UV radiation (Cameron & Robinson 1989a). It implies at the same time that the Balmer lines of RX J1508.6−4423 are not strongly saturated, with an Hα core optical depth of order unity. Although not strictly true, we will nevertheless make the simplifying assumption that the Balmer lines are optically thin. The case B recombination described by Osterbrock (1989) is thus the one most relevant to our situation where Lyman lines and continuum are optically thick while Balmer lines are optically thin.

From Fig. 13, we estimate that the prominences are confined to a torus of radius $1.65\,R_*$ and circular cross-section of diameter $0.7\,R_*$, and thus occupy a volume of about 2×10^{33} cm^3. Moreover, since RX J1508.6−4423 is hotter than AB Dor and its prominences are located closer to the stellar surface, we can safely assume that the electron temperature in the clouds is higher than in AB Dor ones (presumably of the order of 10 000 K), and thus that H is fully ionized. Given that RX J1508.6−4423 is 150 pc away from the Earth, the average Hα and Hβ fluxes we measure (see above paragraph) translate into an average H number densities of about 3×10^{10} cm^{-3}. In this context, we conclude that the total mass in the prominence system is about 10^{20} g (or $5 \times 10^{-14}\,M_\odot$).

The magnetic field B needed to hold the prominence atop coronal loops can be estimated by stating that the magnetic tension at the top of the loop exceeds the local effective gravity $g_{\rm eff}$ acting on the gas (including centrifugal acceleration and thus directed outwards outside of the corotation radius), yielding the following expression:

$$\frac{B^2}{4\pi r_{\rm c}} \geq \rho g_{\rm eff},$$

where $r_{\rm c}$ is the radius of curvature at the top of the loop (taken as $0.3\,R_*$), and ρ the mass density in the prominences (equal to about 5×10^{-14} g cm^{-3}). Assuming that the photospheric field cannot exceed the equipartition value of about 1.5 kG, we conclude that clouds cannot be locked in corotation further than about $4.4\,R_*$. This is in agreement with our reconstructed Doppler maps in Fig. 13, which show no high-contrast azimuthally confined structure outside of a radius of about $3\,R_*$.

From our observation that the whole prominence system is regenerated in less than 4 d (see Section 6), we can also derive an upper limit for the rotational braking time-scale in post T Tauri stars. Using a total prominence mass of 10^{20} g and a maximum radius of $4.4\,R_*$ at which corotation can be enforced, we find that the angular momentum loss of the star is at least 10^{34} dyn cm. Given the total angular momentum of RX J1508.6−4423 at present time (equal to about 4×10^{50} g cm^2 s^{-1}), we conclude that the magnetic braking time-scale is less than 1 Gyr. We emphasize that this estimate is only an upper limit (at least because the typical prominence lifetime is very likely shorter than 4 d) and could be easily as small as 500 Myr. Given the typical spindown time of about 100 Myr derived from observations of rapidly rotating G stars in young clusters at an age of about 25 Myr (e.g. Bouvier et al. 1997), this confirms the suggestion of Cameron & Robinson (1989a,b) that prominence expulsion is indeed a mechanism which participates significantly to the rotational braking of post T Tauri stars.

ACKNOWLEDGMENTS

We thank J. Bouvier for bringing to our attention the newly discovered post T Tauri stars in the Lupus star-forming region, as well as C. Catala for very valuable discussions about various questions raised in this paper. We are also very grateful to R. Jeffries, the referee, for suggesting several modifications that clarified and improved the manuscript.

REFERENCES

Applegate J. H., 1992, ApJ, 385, 621
Barnes J. R., Cameron A. C., James D. J., Donati J.-F., 2000, MNRAS, 314, 162
Barnes J. R., Cameron A. C., Unruh Y. C., Donati J.-F., Hussain G. A. J., 1998, MNRAS, 299, 904
Beuermann K., Baraffe I., Hauschildt P., 1999, A&A, 348, 524
Bouvier J., Forestini M., Allain S., 1997, A&A, 326, 1023
Brown S. F., Donati J.-F., Rees D. E., Semel M., 1991, A&A, 250, 463
Cameron A. C., 1992, in Byrne P. B., Mullan D. J., eds, Surface Inhomogeneities on Late-Type Stars. Springer, Berlin, p. 33
Cameron A. C., Robinson R. D., 1989a, MNRAS, 236, 57
Cameron A. C., Robinson R. D., 1989b, MNRAS, 238, 657
D'Antona F., Mazzitelli I., 1994, ApJS, 90, 467
Donati J.-F., 1999, MNRAS, 302, 457
Donati J.-F., Brown S. F., 1997, A&A, 326, 1135
Donati J.-F., Cameron A. C., 1997, MNRAS, 291, 1
Donati J.-F. et al., 1992, A&A, 265, 682
Donati J.-F., Henry G. W., Hall D. S., 1995, A&A, 293, 107
Donati J.-F., Semel M., Carter B. D., Rees D. E., Cameron A. C., 1997, MNRAS, 291, 658
Donati J.-F., Cameron A. C., Hussain G. A. J., Semel M., 1999, MNRAS, 302, 437
Donati J.-F., Hussain G. A. J., Cameron A. C., Semel M., López Ariste A., Carter B. D., Mengel M., Rees D. E., 2000, MNRAS, submitted
Forestini M., 1994, A&A, 285, 473
Hall D. S., 1991, in Tuominen I., Moss D., Rüdiger G., eds, Proc. IAU Colloq. 130, The Sun and Cool Stars: Activity, Magnetism, Dynamos. Springer, Berlin, p. 353
Herbig G. H., 1978, in Mirzoyan L. V., ed., Problems of Physics and Evolution of the Universe. Armenian Acad. Sci., Yerevan, p. 171
Kitchatinov L. L., Rüdiger G., 1995, A&A, 299, 446
Kitchatinov L. L., Rüdiger G., 1999, A&A, 344, 911
Krautter J., Wichmann R., Schmitt J.H.M.M., Alcala J. M., Neuhaeuser R., Terranegra L., 1997, A&AS, 123, 329
Kurucz R. L., 1993, CDROM # 13 (ATLAS9 atmospheric models) and # 18 (ATLAS9 and SYNTHE routines, spectral line database)
Lanza A. F., Rodonò M., Rosner R., 1998, MNRAS, 296, 893
Marsh T. R., Horne K., 1988, MNRAS, 235, 269
Montes D., Saar S. H., Cameron A. C., Unruh Y. C., 1999, MNRAS, 305, 45
Morossi C., Franchini M., Malagnini M. L., Kurucz R. L., Buser R., 1993, A&A, 277, 173
Osterbrock D. G., 1989, Astrophysics of Gaseous Nebulae and AGNs. University Science Books, Mill Valley, CA
Rucinski S. M., 1987, PASP, 99, 288
Schüssler M., Caligari P., Ferriz-Mas A., Solanki S. K., Stix M., 1996, A&A, 314, 503
Skilling J., Bryan R. K., 1984, MNRAS, 211, 111
Smith M., 1994, A&A, 287, 523
Stellmacher G., Wiehr E., 1994, A&A, 290, 655
Wichmann R., Krautter J., Covino E., Alcala J. M., Neuhaeuser R., Schmitt J. H. M. M., 1997, A&A, 320, 185
Wichmann R., Bouvier J., Allain S., Krautter J., 1998, A&A, 330, 521
Wichmann R., Covino E., Alcala J. M., Krautter J., Allain S., Hauschildt P. H., 1999, MNRAS, 307, 909

This paper has been typeset from a TEX/LATEX file prepared by the author.